Multi-Objective Optimization of Interior Permanent Magnet Machine for Heavy-Duty Vehicle Direct-Drive Applications

Jinghua Ji, Yanjiao Yang, Zhijian Ling, Wenxiang Zhao, *Senior Member*, *IEEE*

Abstract—In this paper, an interior permanent magnet (IPM) machine is presented and optimized for heavy-duty vehicle direct-drive applications. Since efficiency decrease and serious heating come along with excessive core loss under flux weakening control, a rotor topology with the combination of the eccentricity structure and magnetic barriers is proposed. The key is to achieve the comprehensive optimization of the proposed rotor topology to satisfy the different requirements under diverse operating points. Then, a multi-objective automatic parallel optimization method is applied, which simultaneously analyzes multi-condition operation without weight coefficients defined artificially. The 3D Pareto solution set is generated by using nature inspired evolutionary algorithm based on the high-precision metal-modals of optimal prognosis, which reduce the needed computation cost significantly. Moreover, the back electromotive force total harmonic distortion, torque and core loss of the optimal machine are analyzed at corresponding operating points. Finally, the finite-element results are validated by experiments based on a prototype machine.

Index Terms—Permanent-magnet machine, core loss, flux weakening control, representative operating points, rotor topology, multi-objective optimization.

I. INTRODUCTION

HEAVY-DUTY vehicles have been widely applied and play an important role in promoting economic construction. The in-wheel machines are gradually used in heavy-duty vehicles for high transmission efficiency [1]-[5]. Interior permanent magnet (IPM) machine is a promising candidate for in-wheel driving machine due to high power density, wide speed range and reliable operation, etc. [6]-[8].

The torque performance is damaged owing to the limitation of the supply voltage and saturation of current controller in the constant power operation area over the base speed. Flux weakening control is usually carried out in order to broaden the speed range and improve the efficiency of the system over the base speed. However, the higher alternating frequencies of the fundamental and harmonic waveforms of the magnetic field leads to larger core loss under a higher speed. The excessive core loss results in the efficiency decrease and serious heating.

The high temperature causes the irreversible demagnetization of the PM and further deteriorates the electromagnetic performance of the machine. The harmonic core loss resulting from the harmonic magneto motive force (MMF) of the PM can be effectively weakened by reasonably improving the stator or rotor geometry of the machine. Then, the core loss can be reduced effectively [9]-[11]. In [12], an asymmetric rotor shape determined by the advanced inverse cosine function was designed to achieve lower core loss in addition to the torque ripple reduction. The magnetic barriers of the IPM machine with a single-layer U-shaped PM geometry was improved to reduce the core loss by 30%, while the maximum torque is dropped under flux weakening control [13]. Accordingly, the combination of the eccentricity structure and magnetic barriers can be introduced to the rotor to decrease the core loss under flux weakening control.

To achieve the desired performance, optimization is an essential step for IPM machines applied in heavy-duty vehicles. Optimization methods in previous studies can be divided into single objective and multi-objective optimization. The single objective optimization method is used to address only one performance index with the potential sacrifice of other performance indices [14], [15]. In [16], a multilevel optimization strategy for efficient multi-objective optimization which contains four objectives was conduct1.5ed for an IPM machine. The rotor pole arc, rotor radius, stator teeth and the air gap of the machine were selected as the design parameters. Generally, the optimization techniques considering either single or multiple objectives are mainly performed for single operating point analysis. However, optimizing the machine for a single operating point might not ensure that the efficiency and other performance indices are meeting the design requirements within the considered driving cycle. In [17], the cyclic representative points identified by k-means clustering method are used to improve the systematic efficiency of IPM machine from four aspects: active material cost, power losses, torque ripple and degree of PM demagnetization. Therefore, representative operating points are necessarily introduced into multi-objective optimization to enhance the overall performance of the machine [18]-[22].

The initial design of the IPM machine in this paper is a referential model provided by optimizing based on finite-element analysis (FEA). Then, a comprehensive framework of multi-objective optimization will be proposed to improve the overall performance of the machine. First, the proposed rotor topology and representative operating points will be given in Section II. Second, a multi-objective automatic parallel optimization method based on metal-modals of optimal

prognosis (MOPs) will be introduced, and a nature inspired evolutionary algorithm will be used to generate the 3D Pareto solution set in Section III. The performance of initial and optimal machines will be compared by simulation results in Section IV. The prototype will be tested to verify the finite-element results in Section V. Finally, conclusions will be made in Section VI.

II. ROTOR TOPOLOGY AND OPERATING POINTS

A. Proposed Rotor Topology

The geometry of the referential machine for optimization research is shown in Fig. 1. The machine adopts the interior single-layer V-typed PM cavity geometry. Comparing with the conventional V-shaped IPM, the proposed rotor topology includes the evolution of the rotor profile and magnetic barriers. For a fair comparison, both rotor topologies are designed with the same PM dimensions, armature core length and minimum air gap length. Moreover, the same 72-slot/12-pole integer-slot stator design with six-phase double-layer distributed windings is employed for both topologies. Therefore, compared with the referential topology, the proposed rotor topology is achieved without introducing any extra cost.

The sketch map of the proposed rotor topology is illustrated in Fig. 2. The outline of the rotor has evolved from a standard circle to the combination of the eccentric and standard arcs. It reduces the harmonic components of the air gap flux density by constructing the uneven gap length. Meanwhile, two magnetic barriers are added to each pair of PMs, which are symmetrical about the radial axis. These barriers play a certain role of magnetic concentration to improve air gap magnetic density. There are eight design parameters selected to be optimized and marked in the sketch map. These are the dimension parameters introduced by the rotor topology evolution, which have different effects on the electromagnetic performance of the machine. The chosen design variables specifications are listed in Table I, where the variation ranges are determined considering the mechanical strength of the magnetic bridge.
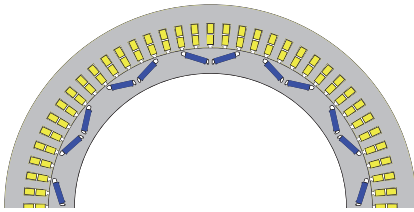

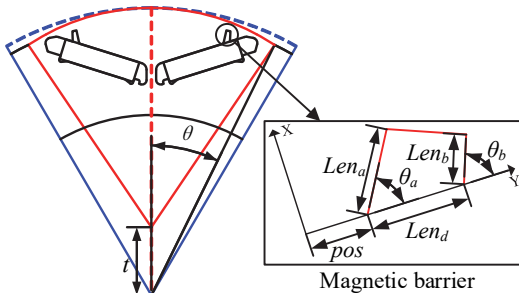Fig. 1. Geometry of the referential machine.

Fig. 2. Sketch map of the design parameters.

TABLE I
DESIGN SPECIFICATION

Design variables	Definitions	Units	Variation ranges
t	Eccentricity distance	mm	[0,100]
θ	Eccentricity angle	deg	[1,14]
pos	Relative position of barriers	mm	[7,9]
Len_d	Width of the bottom of the magnetic barrier	mm	[0.4,1.5]
Len_a	Length of A side	mm	[1.3,3.5]
Len_b	Length of B side	mm	[1.3,3.5]
θ_a	Tilt angle of A side	deg	[30,90]
θ_b	Tilt angle of B side	deg	[30,90]

B. Selection of Operating Points

Compared with the traditional light vehicles, the heavy-duty vehicles have complex driving conditions, which are different from the design requirements of both traditional road application vehicles and field operation engineering vehicles. Therefore, three low-speed zones and one high-speed zone are taken as the driving cycle referred from the Chinese common bus operating conditions. According to the power of the IPM machine and the basic vehicle parameters of the heavy-duty vehicle, the simulation model of the vehicle is developed. Then, the torque-speed curve of the machine is obtained from the driving cycle data. The Fuzzy C-means clustering algorithm is used to automatically classify the sample points to obtain the clustering centers, as shown in Fig. 3. Finally, a center point at 7113 r/min is selected to represent the operation of the machine under flux weakening control.

Based on the importance for wide speed regulating system and traction machine, three representative operating points including unload point, rated point and flux weakening point are selected to be analyzed in this paper. The machine designed for heavy-duty vehicle is required to work continuously under rated load and perform for a certain time under higher speed. The allowable range of the temperature rise of the machine must be ensured. It should be noted that the temperature rise is closely related to the loss of the machine. Consequently, the reduction of the stator and rotor core loss at high speed under flux weakening control is focused on. Meanwhile, the electromagnetic performance under no-load condition and the torque capability under rated load are considered. Table II lists the features of the referential machine under diverse operating conditions.

TABLE II
FEATURES OF THE THREE OPERATING POINTS

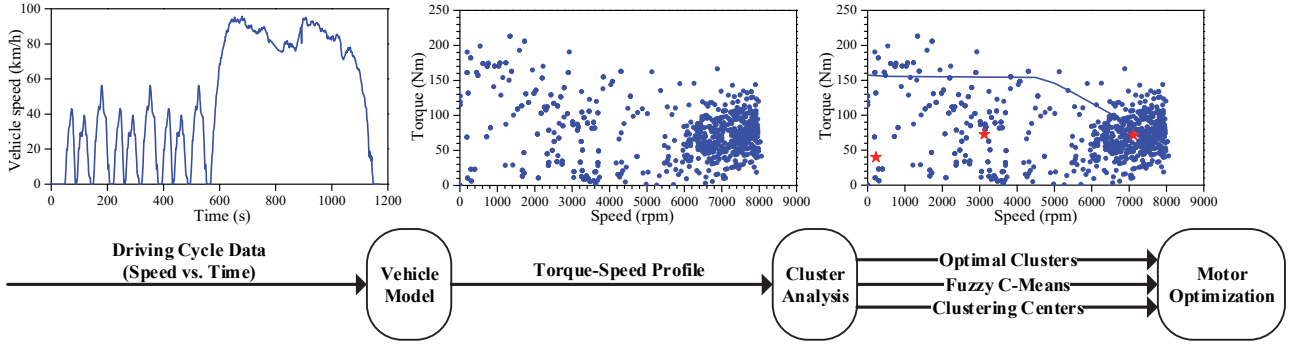| Points	Imax	Gamma	Speed	T_{avg}
	A	deg	r/min	Nm
S_1	0	0	1000	0
S_2	19	30	1000	79
S_3	31.8	68.5	7113	78

Fig. 3. Flowchart of clustering centers selection.

C. Core Loss Analysis

A classical model for core loss calculation is based on the Bertotti discrete model. Based on the principle of harmonic analysis, the flux density at any point of the machine can be decomposed into fundamental and a series of harmonic components after Fourier expansion. The harmonic components bring an enormous amount of core loss in stator. The time-variation magnetic field analysis reveals that the magnetization of different points is different. The magnetic field in middle part of stator teeth can be roughly considered as alternating magnetic field, while other parts are elliptic rotating field. Therefore, the elliptical magnetic field can be decomposed into two orthogonal alternating magnetic field. The total core loss generated by the elliptical magnetic field is equal to the sum of core loss produced by radial and tangential alternating magnetic field.

Core losses, including the hysteresis loss component, the eddy current loss component and the excess loss component in core laminations, can be approximately expressed as

$$
\begin{aligned}
P_{Fe} &= P_h + P_c + P_e \\
&= k_h \sum_k^N (kf)\left(B_{rk}{}^x + B_{tk}{}^x\right) \\
&\quad + k_c \sum_k^N (kf)^2\left(B_{rk}{}^2 + B_{tk}{}^2\right) \\
&\quad + k_e \sum_k^N (kf)^{1.5}\left(B_{rk}{}^{1.5} + B_{tk}{}^{1.5}\right)
\end{aligned}
\tag{1}
$$

where k_h, k_c, k_e are the coefficients of the hysteresis losses, eddy current losses and excess losses, respectively. B_{rk}, B_{tk} are the radial and tangential amplitudes of the kth-order harmonic, f is the frequency, and x is the Steinmetz coefficient, which is usually 1.6.

For the referential IPM machine, the flux density waveform of stator teeth is distorted with the change of load condition. The harmonic eddy current losses become the major core loss at the high rotation speed under flux weakening control. In flux-weakening and high-speed region, the fundamental and harmonic components of stator teeth flux density are achieved under radial and tangential alternating magnetic field, respectively. They are compared before and after adopting the optimized rotor topology, as shown in Figs. 4(a) and 4(b). The magnitudes of the higher harmonics have an obvious trend to be weakened after adopting the optimized rotor topology.

In addition to the effects of the stator slot harmonics, the distortion of the air gap flux density waveform is closely related to the flux density waveform at the stator teeth. Both are affected by the harmonic MMF of the PM. In Fig. 4(c), the magnitudes of the 30th and 42nd order harmonic components of the air gap flux density are effectively weakened after adopting the optimized rotor topology under flux weakening control.
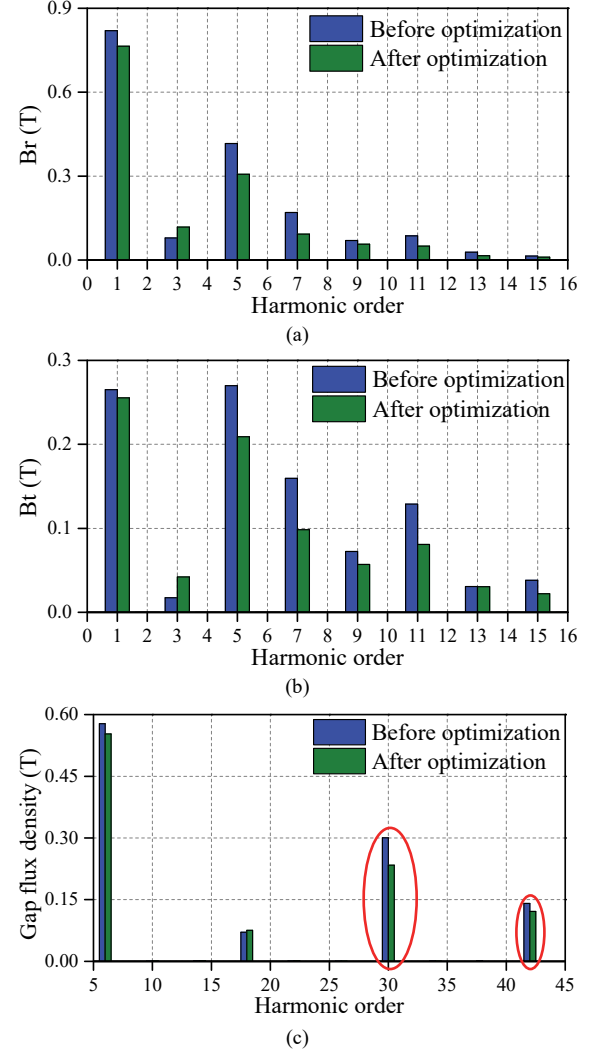

Fig. 4. Harmonic analysis under flux weakening control. (a) Stator teeth flux density comparison under radial alternating magnetic field. (b) Stator teeth flux density comparison under tangential alternating magnetic field. (c) Air gap flux density comparison.

III. MULTI-OBJECTIVE OPTIMIZATION

A. Flowchart of Optimization Approach

The comprehensive multi-objective optimization framework of the proposed rotor structure is constructed in Fig. 5. It can be divided into four parts, namely operating points performance, variables and objectives determination, eccentricity structure optimization and magnetic barriers optimization. During the process, the position of the barriers is determined by establishing the relative coordinate with reference to the position of the PMs. Also, the PMs move slightly with the changes of the eccentricity parameters. Therefore, the two shapes are optimized in turn.
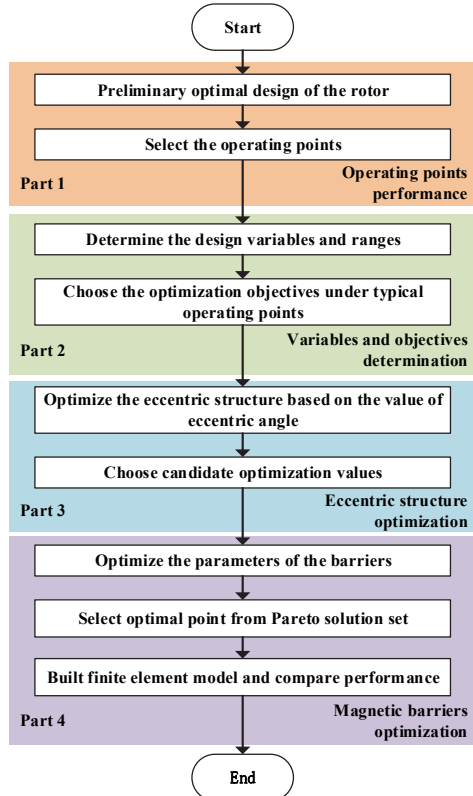

Fig. 5. Framework of the multi-objective optimization approach.

In part 1, according to the reference driving cycle of the heavy-duty vehicle, a representative operating point under flux weakening control is selected by Fuzzy C-means clustering method. The representative flux weakening point along with unload point and rated point are analyzed. Then, based on typical operating conditions, the FEA of the proposed machine is carried out.

In part 2, on the basis of the different design requirements at diverse operating points, some important optimization objectives under corresponding operation condition are selected. These objectives are completely different and have diverse emphases. The design variables and the corresponding ranges are also determined simultaneously. Based on correlation evaluation, the design variables are optimized step by step.

In part 3, according to the requirements of rotor mechanical stress, the optimization of the eccentricity structure is divided into two cases based on the value of the eccentricity angle. The position of PMs is a slightly affected by the eccentricity distance. Accordingly, the eccentricity structure is optimized at first. The optimization process used in this work is multi-objective automatic parallel optimization with conventional steps.

In part 4, based on the candidate optimal design of the eccentricity structure, the optimization of the magnetic barriers continued in the same way. The Pareto solution set will be generated by a multi-objective genetic algorithm method. Next, the optimal design will be selected from the Pareto solution set and build the finite-element model to compare with the results from the original model.

B. Correlation Evaluation

The abovementioned electromagnetic models under various operating conditions are integrated into the main optimization program. The optimization process is shown in Fig. 6. The major optimization time focuses on the joint FEA for global correlation evaluation. The required computation cost depends on the computer capacity and sample size. Compared with the conventional multi-objective optimization method, the joint FEA simplify the settings of the sampling to reduce extra cost on data processing. Moreover, the optimization objectives under three representative operating points are calculated simultaneously without being transformed into a single objective function by weight coefficients defined artificially.
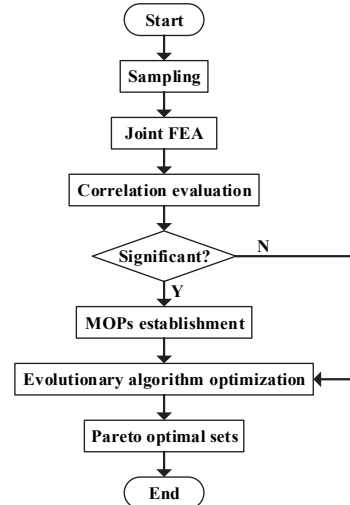

Fig. 6. Illustration of the optimization process.

For the proposed model, the core loss is set as the main objective under flux weakening control to avoid efficiency decrease and serious heating. Under the rated load, the performance of the output torque and torque ripple usually need to be paid more attention. Then, the total harmonic distortion of no-load back electromotive force (EMF) is closely related with the electromagnetic performance. Thus, the design objective is to minimize the total harmonic distortion of no-load back EMF THD_U, the torque ripple under rated load T_{rip} and the core loss under flux weakening control P_{Fe}. Meanwhile, the average torque under rated load T_{avg} should be as large as possible, while the variation cannot be less than 10% of the referential

torque. The total harmonic distortion of no-load back EMF THD_U and the torque ripple T_{rip} can be expressed as:

$$THD_U = \frac{\sqrt{\sum_{n=2}^{\infty} E_n^2}}{E_1} \times 100\% \tag{2}$$

$$T_{rip} = \frac{T_{max} - T_{min}}{T_{avg}} \times 100\% \tag{3}$$

where E_1 is the fundamental voltage, E_n is the n-th harmonic voltage and T_{max}, T_{min} are the maximum, minimum values of output torque, respectively.

The Advanced Latin Hypercube Sampling (ALHS) was used to obtain the experimental sample group based on the variation ranges of the design variables. The ALHS is an improved design of experiment technique. Based on the existing Latin Hypercube sampling set, the random evolution algorithm was used to add optimized samples to minimize the correlation of sample points. The sampling process has been illustrated in Fig. 7. The sample size is defined according to the actual needs. The variation ranges of the design variables are divided into subintervals equally. One sampling point are randomly selected for each subinterval. The whole design variable space is more fully explored in the case of a small number of points. The selected points are mapped into standard normal distribution samples through the inverse function of standard normal distribution. Finally, the sampling sequence is disrupted and generated.

The distribution of sample points of the eccentricity structure optimization with θ less than 11 degrees is shown in Fig. 8. There are 30 experiment runs calculated by joint simulation with FEA solver. The total computation time is about 3.5 hours for a 64 bits computer of Inter I7 2.6GHz CPU with 8 GB RAM. Then, the correlation coefficients between parameters are calculated based on the simulation results which can be given by:

$$\rho(X_i, Y_j) = \frac{1}{N-1} \frac{\sum_{i=1}^{N}(X_i - \hat{\mu}_X)(Y_j - \hat{\mu}_Y)}{\hat{\sigma}_X \hat{\sigma}_Y} \tag{4}$$

where Y_j is the j-th optimization objective, X_i is the design parameters, and N is the sample size.

Global correlation matrix shows correlation of each optimization objective with respect to design variables, as listed in Table III. Both the eccentricity distance and the eccentricity angle are the key parameters to the optimization objectives when eccentricity angle is less than 11 degrees. Otherwise, only the eccentricity distance influences the optimization objectives greatly and the eccentricity angle was artificially transmitted to the optimization of magnetic barriers. The same sensitivity analysis method was used for optimization of magnetic barriers. In the algorithm optimization, the nonsignificant variables are automatically filtered out. But they should be limited by the constrains and be closely correlated with significant variables.

The correlation coefficients of different optimization objectives are listed in Table III. As exhibited, the correlation coefficient between average torque and torque ripple is 0.98.

The two optimization objectives are highly positively correlated. This reveals the contradictions that the lower torque ripple is obtained at the expense of torque capability. The correlation coefficients among different optimization objectives also verify the necessity of multi-objective optimization.
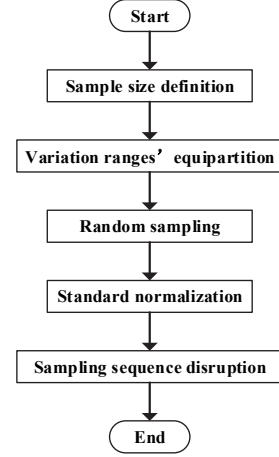

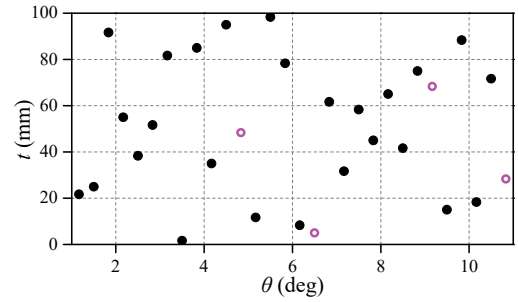Fig. 7. Flowchart of ALHS sampling process.

Fig. 8. Distribution of experimental points in ALHS.

TABLE III
CORRELATION MATRIX

ρ	θ	t	THD_U	T_{avg}	T_{rip}	P_{Fe}
θ [deg]	1	0.04	0.53	-0.66	-0.71	-0.75
t [mm]	0.04	1	0.62	-0.67	-0.63	-0.68
THD_U [%]	0.53	0.62	1	-0.89	-0.82	-0.86
T_{avg} [Nm]	-0.66	-0.67	-0.89	1	0.98	0.97
T_{rip} [%]	-0.71	-0.63	-0.82	0.98	1	0.98
P_{Fe} [kW]	-0.75	-0.68	-0.86	0.97	0.98	1

C. Optimization based on MOPs

Multi-objective optimization algorithms usually work upon high-precision mathematical models. In this case, the MOPs were established based on the joint simulation results of sample points. The unimportant variables are removed according to the correlation evaluation to improve the quality of the precision models when conducting the MOPs. The approximation accuracy of the mathematical models is quantified by the coefficient of prediction *CoP*, which is defined as:

$$CoP = 1 - \frac{\sum_{i=1}^{N}(Y_i - \hat{Y}_i)^2}{\sum_{i=1}^{N}(Y_i - \mu_Y)^2} \tag{5}$$

where Y_i and $\hat{Y}_i$ are the values of objectives obtained from FEA and prediction model. μ_Y is the average value of Y_i, and N is the sample size. Compared with traditional coefficient of determination CoD, the phenomenon of false accuracy will not appear by CoP in the case of small sample size. The MOPs for each objective versus two significant variables are shown in Fig. 9.

A multi-objective nature inspired evolutionary algorithm optimization method is applied to the MOPs of THD_U, T_{avg}, T_{rip} and P_{Fe}, respectively. It can obtain a set of Pareto optimal solutions within 60 seconds. The 3D Pareto plot of the three main objectives can be obtained in a short run, as shown in Fig. 10. Except for some unreasonable points, several optimized points can be selected from the optimal set which are marked red. Considering the constraints of the average torque under rated load T_{avg}, the final optimization result is exhibited in Table IV.
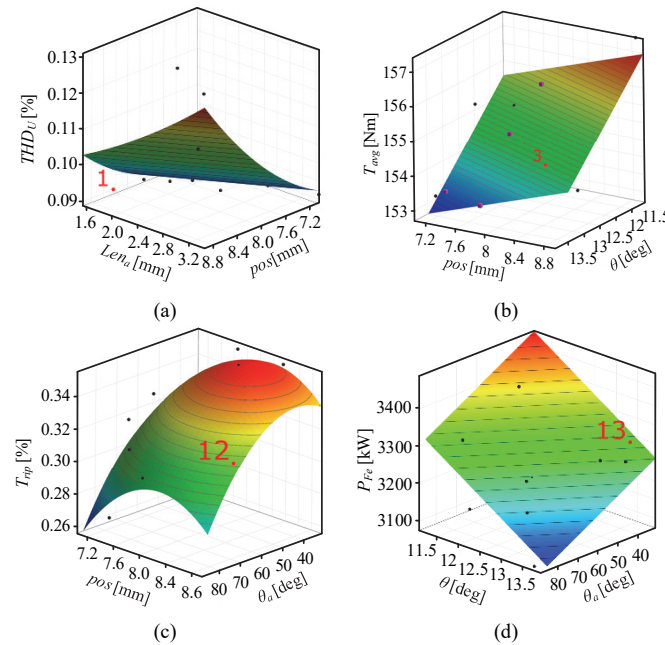
TABLE IV
FINAL OPTIMIZATION RESULTS

	Par.	Unit	Final optimized
Eccentricity structure	t	mm	22.8
	θ	deg	14
Magnetic barriers	pos	mm	7.1
	Len_d	mm	1.2
	Len_a	mm	2.4
	Len_b	mm	1.5
	θ_a	deg	89.9
	θ_b	deg	86
Optimization objectives	THD_U (S_1)	%	9.8
	T_{avg} (S_2)	Nm	72.7
	T_{rip} (S_2)	%	31.0
	P_{Fe} (S_3)	kW	3.3

Fig. 9. MOPs of objectives versus two significant variables. (a) THD_U distribution between Len_a and pos. (b) T_{avg} distribution between pos and θ. (c) T_{rip} distribution between pos and θ_a. (d) P_{Fe} distribution between θ and θ_a.
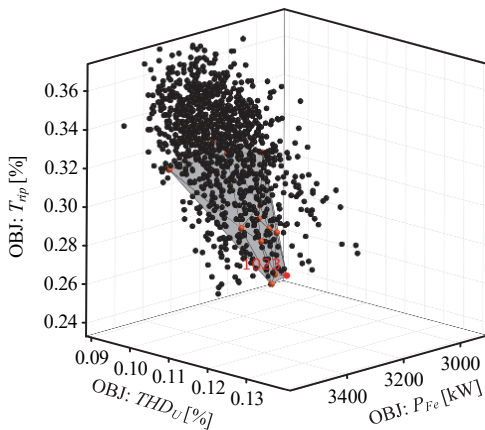
Fig. 10. 3D Pareto optimal sets of objectives.

IV. EVALUATION OF MACHINE PERFORMANCE

To verify the validity of the optimization approach for the proposed rotor structure, the electromagnetic performance of initial and optimal models are evaluated by FEA. Fig. 11(a) shows the no-load back EMF waveforms of the initial and the optimal machine. The waveform of the optimal machine is more symmetrical and sinusoidal than the initial one. It can be calculated according to (2), the THD_U of the initial and optimal machines is 11.2% and 9.8%, respectively, which has decreased by 12.5%. Fig. 11(b) depicts the cogging torque waveforms of the initial and the optimal machines. It can be seen that the peak-to-peak value of the initial machine is 23.5 Nm. After multi-objective optimization of the proposed rotor topology, the value falls to 16 Nm which results in lower torque ripple at rated load.

The output torque waveforms of two machines at rated work point are compared in Fig. 12. The results illustrate that the optimal machine can offer more stable load torque under the same current excitation than the initial one. The torque ripple T_{rip} of the optimal machine is 31.0%, whereas the torque ripple of the initial one is 54.3%. Moreover, it is acceptable that the average value of output torque decreases from 78.8 Nm to 72.7 Nm.

The waveforms of the total core loss of both stator and rotor under flux weakening control in single cycle are shown in Fig. 13. The average value of the core loss decreases from 5.3 kW of the initial machine to 3.3 kW of the optimal one by 38%. Fig. 11(c) depicts that the 30th and 42nd order harmonic components of the air gap flux density are decreased by the optimization which is consistent with the core loss analysis in Section II. Since the harmonic core loss is directly proportional to the square of harmonic order and amplitude, the increase of 18th order harmonic has less reaction to the reduction of core loss than the decrease of 30th and 42nd order harmonics.

Employing the combination of the eccentricity structure and magnetic barriers also leads to concerns about weakening of rotor mechanical strength. The material adopted for the rotor core is B35AH230 and the yield strength is 400 MPa. Fig. 14

compares the Mises stress distribution on rotors at 7113 r/min. The maximum Mises stress on the rotor core is 183.46 MPa for the referential IPM machine, while that for the optimal IPM machine is 209.78 MPa. The location of maximum Mises stress point on the optimal rotor is different from that of the referential one. It confirms that maximum stress of the optimal machine is similar to that in the initial machine. The maximum stresses are far less than the yield strength.

The comprehensive comparisons between the initial and the optimal IPM machine under three typical operating points are given in Table V. It can be concluded that the optimal machine has a significant decrease in rated torque ripple and core loss under flux weakening control. Besides, the total harmonic distortion of no-load back EMF has been decreased. Thus, the optimized rotor topology has improved the electromagnetic performance of the IPM machine for heavy-duty vehicle direct-drive applications.
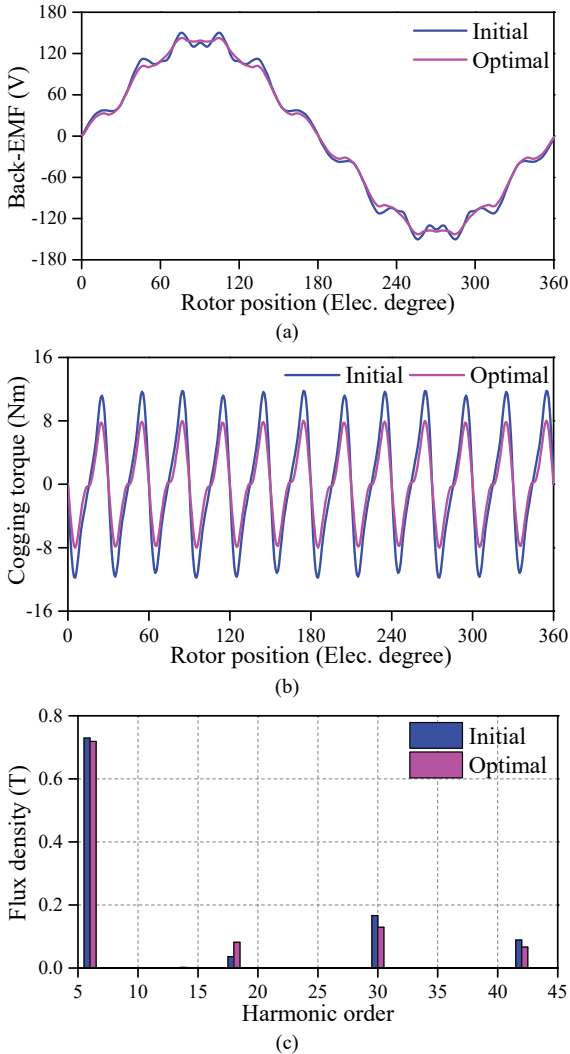

(a)

(b)

(c)

Fig. 11. Comparison under no-load condition. (a) Back EMF waveforms. (b) Cogging torque waveforms. (c) Harmonic analysis of air gap flux density.
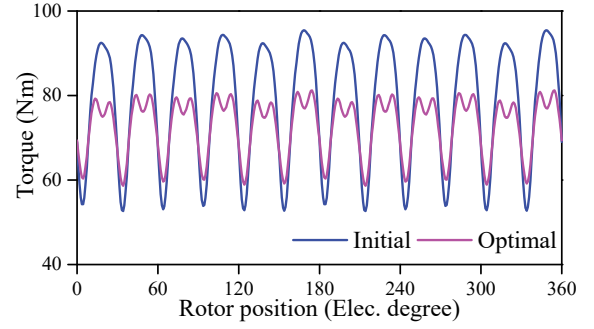

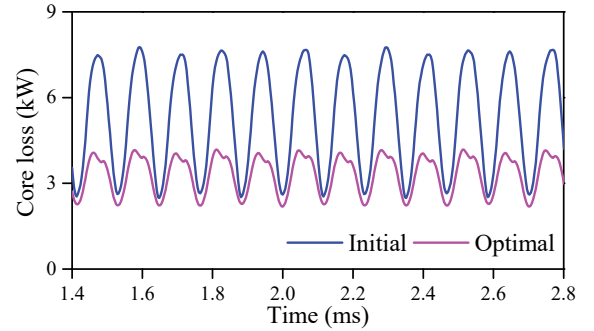Fig. 12. Comparison of output torque at rated load.

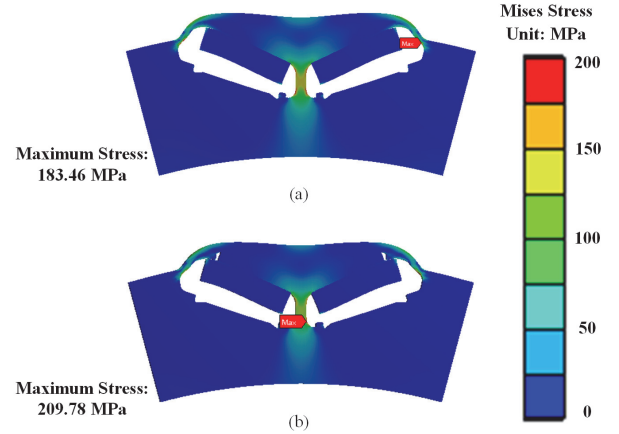Fig. 13. Comparison of core loss under flux weakening control.

Fig. 14. Mises stress distribution at 7113 r/min when Young's modulus is 120 GPa, density is 7850 kg/m3, Poisson's ratio is 0.3 and Yield strength is 400 MPa for rotor core. (a) The referential IPM machine. (b) The optimal IPM machine.

TABLE V
MACHINE PERFORMANCE

Points	Objectives	Initial machine	Optimal machine
S_1	THD_U [%]	11.2	9.8
S_2	T_{rip} [%]	54.3	31.0
	T_{avg} [Nm]	78.8	72.7
S_3	P_{Fe} [kW]	5.3	3.3

V. EXPERIMENT RESULTS

In order to verify the accuracy of the finite-element calculation, a prototype of the referential IPM machine is designed and manufactured. Fig. 15 shows the prototype IPM machine and the experiment platform. The test prototype is

connected in series with the load, mechanically, by coaxial driving. With experimental data, FEA results have been compared on the unload back EMF and rated torque curve.

The phase back EMF of the prototype machine at open-circuit is measured. Fig. 16(a) shows the test back EMF waveform of the prototype compared with the predicted ones. The measured back EMF waveform has little difference with the FEA ones according to the spectrum shown in Fig. 16(b).

The finite-element and measured results of the rated torque are compared in Fig. 17. The average torque of the prototype is similar to the predicted one. There is a slight deviation from the FEA results in terms of the average torque and torque ripple, which is within the acceptable experimental error.
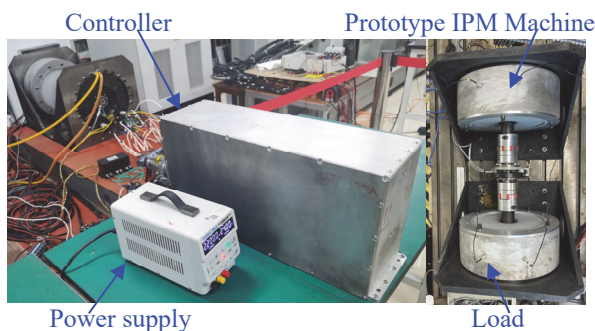

Fig. 15. Experiment platform of the prototype.
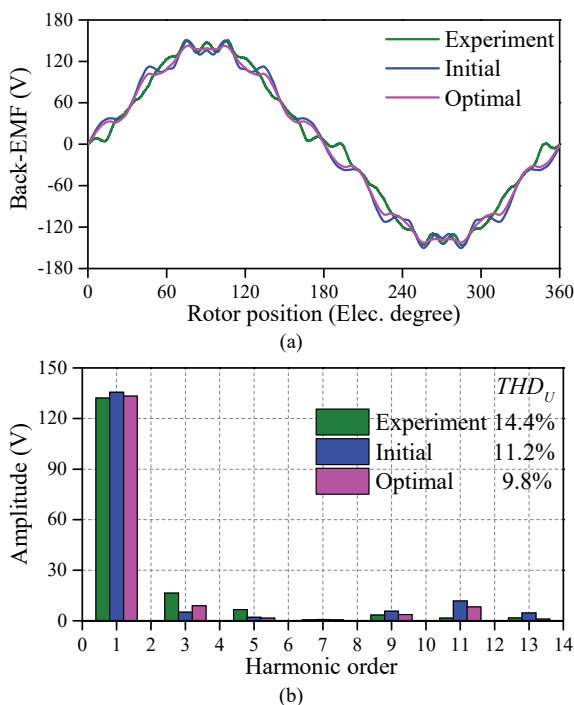

(a)

(b)

Fig. 16. Comparison between predicted and measured back EMF waveforms. (a) Waveforms. (b) Spectrum.
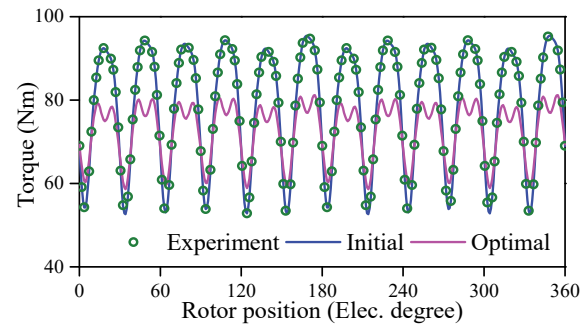

Fig. 17. Experimental and predicted rated torque waveforms.

VI. CONCLUSION

In this paper, a comprehensive framework of multi-objective automatic parallel optimization for the IPM machine has been proposed to satisfy the different requirements under diverse operating points. In order to reduce the excessive core loss under flux weakening control, the eccentricity structure and magnetic barriers have been designed and optimized. The Fuzzy C-means clustering analysis method is adopted, and three representative points have been selected as the no-load point, rated point, and flux weakening point, respectively. The optimization process is mainly composed of correlation evaluation, establishing the MOPs and optimization based on nature inspired evolutionary algorithm. Then, the back EMF total harmonic distortion, torque and core loss of the optimal machine have been compared with the initial one by FEA at corresponding operating points. The results reveal that the optimal machine possesses less core loss under flux weakening control and lower torque ripple under rated load than the initial one. Meanwhile, the optimal IPM machine puts forward high requirements for processing and manufacturing technology. There are many unavoidable variations for the design parameters of the optimal IPM machine in the production due to the practical manufacturing tolerances, material diversities and assembling uncertainties. In future research, robust design optimizations will be developed to try these challenges. Finally, a prototype has been tested to validate the referential machine performance. Both the simulation and experimental results verified the feasibility of the multi-objective optimization method implemented on the IPM machine for heavy-duty vehicle direct-drive applications.

REFERENCES

[1] H. Zhang, W. Hua, D. Gerada, Z. Xu, and C. Gerada, "Analytical model of modular spoke-type permanent magnet machines for in-wheel traction applications," *IEEE Trans. Energy Conv.*, vol. 35, no. 3, pp. 1289-1300, Sep. 2020.

[2] H. Chen, X. Liu, N. A. O. Demerdash, A. M. EL-Refaie, J. Zhao, and J. He, "Comparison and design optimization of a five-phase flux-switching PM machine for in-wheel traction applications," *IEEE Trans. Energy Conv.*, vol. 34, no. 4, pp. 1805-1817, Dec. 2019.

[3] H. Zhang, W. Hua, D. Gerada, C. Gerada, Y. Li, and G. Zhang, "Comparative study on two modular spoke-type PM machines for in-Wheel traction applications," *IEEE Trans. Energy Conv.*, vol. 34, no. 4, pp. 2137-2147, Dec. 2019.

[4] Y. Sun, W. Zhao, J. Ji, J. Zheng, and X. Song, "Effect of phase shift on inductance and short-circuit current in dual three-phase 48-slot/22-pole permanent-magnet machines," *IEEE Trans. Ind. Electron.*, vol. 69, no. 2, pp. 1135-1145, Feb. 2022.

[5] S. Zhu, W. Zhao, G. Liu, Y. Mao, and Y. Sun, "Effect of phase shift angle on radial force and vibration behavior in dual three-phase PMSM," *IEEE Trans. Ind. Electron.*, vol. 68, no. 4, pp. 2988-2998, Apr. 2021.

[6] Y. Xiao, Z. Q. Zhu, S. S. Wang, and *et al*., "A novel asymmetric interior permanent magnet machine for electric vehicles," *IEEE Trans. Energy Conv.*, vol. 36, no. 3, pp. 2404-2415, Sep. 2021.

[7] R. Dutta, A. Pouramin, and M. F. Rahman, "A novel rotor topology for high-performance fractional slot concentrated winding interior permanent magnet machine," *IEEE Trans. Energy Conv.*, vol. 36, no. 2, pp. 658-670, Jun. 2021.

[8] G. Liu, L. Liu, Q. Chen, and W. Zhao, "Torque calculation of five-phase interior permanent magnet machine using improved analytical method," *IEEE Trans. Energy Conv.*, vol. 34, no. 2, pp. 1023-1032, Jun. 2019.

[9] Q. Li, T. Fan, and X. Wen, "Characterization of iron loss for integral-slot interior permanent magnet synchronous machine during flux weakening," *IEEE Trans. Magn.*, vol. 53, no. 5, May 2017, Art no. 8101308.

[10] M. Seo, Y. Ko, T. Lee, Y. Kim, and S. Jung, "Loss reduction optimization for heat capacity improvement in interior permanent magnet synchronous machine," *IEEE Trans. Magn.*, vol. 54, no. 11, Nov. 2018, Art no. 8207705.

[11] D. Žarko, and T. Jerčić, "Novel empirical model for calculation of core losses in permanent magnet machines," *IEEE Trans. Energy Conv.*, vol. 35, no. 1, pp. 248-259, Mar. 2020.

[12] Y. Jung, M. Lim, M. Yoon, J. Jeong, and J. Hong, "Torque ripple reduction of IPMSM applying asymmetric rotor shape under certain load condition," *IEEE Trans. Energy Conv.*, vol. 33, no. 1, pp. 333-340, Mar. 2018.

[13] C. Xia, L. Guo, Z. Zhang, T. Shi, and H. Wang, "Optimal designing of PM cavity to reduce iron loss of interior permanent magnet machine," *IEEE Trans. Magn.*, vol. 51, no. 12, Dec. 2015, Art no. 8115409.

[14] W. Zhao, A. Ma, J. Ji, X. Chen, and T. Yao, "Multi-objective optimization of a double-side linear vernier PM machine using response surface method and differential evolution," *IEEE Trans. Ind. Electron.*, vol. 67, no. 1, pp. 80-90, Jan. 2020.

[15] W. Zhao, T. Yao, L. Xu, X. Chen, and X. Song, "Multi-objective optimization design of a modular linear permanent-magnet vernier machine by combined approximation models and differential evolution," *IEEE Trans. Ind. Electron.*, vol. 68, no. 6, pp. 4634-4645, Jun. 2021.

[16] X. Sun, Z. Shi, G. Lei, Y. Guo, and J. Zhu, "Multi-objective design optimization of an IPMSM based on multilevel strategy," *IEEE Trans. Ind. Electron.*, vol. 68, no. 1, pp. 139-148, Jan. 2021.

[17] A. Fatemi, N. A. O. Demerdash, T. W. Nehl, and D. M. Ionel, "Large-scale design optimization of PM machines over a target operating cycle," *IEEE Trans. Ind. Appl.*, vol. 52, no. 5, pp. 3772-3782, Sept.-Oct. 2016.

[18] B. D. S. G. Vidanalage, M. S. Toulabi, and S. Filizadeh, "Multimodal design optimization of V-shaped magnet IPM synchronous machines," *IEEE Trans. Energy Conv.*, vol. 33, no. 3, pp. 1547-1556, Sep. 2018.

[19] X. Zhu, D. Fan, L. Mo, Y. Chen, and L. Quan, "Multi-objective optimization design of a double-rotor flux-switching permanent magnet machine considering multimode operation," *IEEE Trans. Ind. Electron.*, vol. 66, no. 1, pp. 641-653, Jan. 2019.

[20] X. Zhou, X. Zhu, W. Wu, Z. Xiang, Y. Liu, and L. Quan, "Multi-objective optimization design of variable-saliency-ratio PM machine considering driving cycles," *IEEE Trans. Ind. Electron.*, vol. 68, no. 8, pp. 6516-6526, Aug. 2021.

[21] G. Xu, Z. Jia, W. Zhao, Q. Chen, and G. Liu, "Multi-objective optimization design of inset-surface permanent magnet machine considering deterministic and robust performances," *Chin. J. Electr. Engin.*, vol. 7, no. 3, pp. 73-87, Sep. 2021.

[22] Y. Mao, S. Niu, and Q. Wang, "Design and optimization of a slot-PM-assisted doubly-salient machine based on saturation assuaging," *Chin. J. Electr. Engin.*, vol. 7, no. 3, pp. 65-72, Sep. 2021.
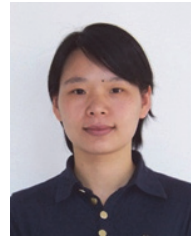
Jinghua Ji received the B.Sc., M.Sc., and Ph.D. degrees in electrical engineering from Jiangsu University, Zhenjiang, China, in 2000, 2003, and 2009 respectively. Since 2000, she has been with the School of Electrical and Information Engineering, Jiangsu University, where she is currently a Professor.

From 2013 to 2014, she was a Visiting Scholar with the Department of Electronic and Electrical Engineering, University of Sheffield, Sheffield, U.K. Her areas of interest include motor design and electromagnetic field computation. She has authored and co-authored over 50 technical papers in these areas.

Yanjiao Yang received the B.Sc. degree in electrical engineering from Jiangsu University, Zhenjiang, China, in 2019, where she is currently working toward the M.Sc. degree in electrical engineering.

Her research interests include optimized design and analysis of permanent magnet machine.

Zhijian Ling received the B. Sc degree in electrical engineering and automation from Shandong Agriculture University, Tai'an, China, in 2013, and the Ph.D. degree in electrical engineering from Jiangsu University, Zhenjiang, China, in 2020. He is currently a Lecturer with the School of Electrical and Information Engineering, Jiangsu University. From September 2018 to August 2019, he was a joint Ph.D. student funded in the Department of Energy Technology, Aalborg University, Aalborg, Denmark.

His research interests include the design and analysis of permanent magnet electrical machines, and electrical actuators.

Wenxiang Zhao (M'08-SM'14) received the B.Sc. and M.Sc. degrees from Jiangsu University, Zhenjiang, China, in 1999 and 2003, respectively, and the Ph.D. degree from Southeast University, Nanjing, China, in 2010, all in electrical engineering.

He has been with Jiangsu University since 2003, where he is currently a Professor with the School of Electrical Information Engineering. From 2008 to 2009, he was a Research Assistant with the Department of Electrical and Electronic Engineering, University of Hong Kong, Hong Kong. From 2013 to 2014, he was a Visiting Professor with the Department of Electronic and Electrical Engineering, University of Sheffield, Sheffield, U.K. He has authored and co-authored over 250 technical papers. His current research interests include electric machine design, modeling, fault analysis, and intelligent control.